ADVANCED MATERIALS
www.advmat.de

Bandgap Tunability in $Zn(Sn,Ge)N_2$ Semiconductor Alloys

Prineha Narang, Shiyou Chen, Naomi C. Coronel, Sheraz Gul, Junko Yano, Lin-Wang Wang, Nathan S. Lewis, and Harry A. Atwater**

The commercial prominence in the optoelectronics industry of tunable semiconductor alloy materials based on nitride semiconductor devices, specifically InGaN, motivates the search for earth-abundant alternatives for use in efficient, high-quality optoelectronic devices and solar energy-conversion systems. We describe the first-principles simulation as well as the synthesis and optoelectronic and spectroscopic characterization of a series of direct band-gap semiconductor alloys, $ZnSn_{1-x}Ge_xN_2$. These materials have a crystal structure and electronic structure similar to that of the InGaN alloys. $ZnSn_{1-x}Ge_xN_2$ alloys with various compositions were synthesized, with the elements fully miscible across the composition range without evidence for phase separation, as shown by X-ray diffraction and X-ray absorption fine-structure spectroscopy. The optical bandgaps of the $ZnSn_{1-x}Ge_xN_2$ alloys range from 2.0 to 3.1 eV, and nitrogen K-edge X-ray absorption and emission spectroscopy showed that the conduction-band minimum shifted to higher energy with the addition of Ge, while the valence-band maximum remained at constant energy. Relatively small values were measured (0.29 eV) and calculated (0.67 eV) for the band-bowing parameters for the bandgaps of the $ZnSn_{1-x}Ge_xN_2$ alloys, indicating that the bandgaps of the $ZnSn_{1-x}Ge_xN_2$ alloy series could be tuned almost monotonically by control of the Sn/Ge ratio.

InGaN-based semiconductor materials have attained commercial prominence in optoelectronics in part due to the large range in electronic bandgaps facilitated by tuning the In/Ga ratio of InGaN alloys.[1] The experimentally determined fundamental gap of GaN is 3.51 eV,[2] while that of InN is 0.69 eV.[3] Hence, InGaN alloys provide a simple class of semiconductors whose fundamental bandgap can, in principle, span the entire visible spectrum and beyond. However the InGaN semiconductors are difficult to synthesize as homogeneous alloys, without phase separation, across the full range of In/Ga ratios. This behavior has limited the compositional range for which InGaN typically exhibits high radiative efficiency, in turn limiting the range of light-emitting, photovoltaic or photoelectrochemical device applications of such materials. The large volume difference between InN and GaN[5] promotes clustering to relieve internal strains, and precludes the straightforward synthesis of high-quality crystals that have sufficiently high In concentrations to produce a bandgap of the alloy in the green range of the color spectrum.[4] Additionally, the reliance on indium, with its limited economically viable sources, could potentially limit the large-scale incorporation of InGaN in solar energy-conversion applications. These factors motivate the search for alternatives to current III-nitride semiconductors for both optoelectronics and solar energy-conversion applications.

The II-IV-N_2 compounds, closely related to the wurtzite-structured III-N semiconductors, have similar electronic and optical properties to InGaN, for example, direct bandgaps and large optical absorption coefficients.[8,20] The choice of different group II and group IV elements provides chemical diversity that can be exploited to tune the structural and electronic properties through the series of alloys. $ZnSnN_2$ ($ZnGeN_2$) can be considered as derived from binary GaN by the replacement of two Ga atoms by Zn+Sn (Zn+Ge) atoms.[6,7] GaN is more stable in the wurtzite structure, therefore $ZnSnN_2$ and $ZnGeN_2$ can crystallize in the wurtzite-derived structure with two primitive cells, (i) the one with the $Pna2_1$ symmetry, shown in **Figure 1**a(ii), and (ii) the one with the $Pmc2_1$ symmetry, shown in Figure 1a of ref.[8] (The two structures can be called wurtzite-chalcopyrite and wurtzite-CuAu, derived from the quaternary I_2-II-IV-VI_4 wurtzite-kesterite and wurtzite-stannite structures respectively through replacing I by Zn, II and IV by Sn, and VI by N[7]). Other structures have larger primitive cells than these two structures and thus can be considered a mixing of these two structures, with intermediate properties.

We report a theoretical investigation of the optoelectronic behaviour of the $ZnSn_xGe_{1-x}N_2$ alloy series, as well as an experimental investigation of the alloy structure and energy-band structure using spectroscopic ellipsometry and X-ray spectroscopy. X-ray diffraction has additionally been used to investigate the phase behavior and composition of this alloy series.

Because our calculations, as well as previous calculations,[8] have shown that the wurtzite-chalcopyrite structure has a lower energy than the wurtzite-CuAu structure, our theoretical investigation of the $ZnSn_xGe_{1-x}N_2$ alloys focused on the wurtzite-chalcopyrite structure, with Sn and Ge randomly distributed on the Sn/Ge sublattice. Calculations of disordered semiconductor

P. Narang,[+] N. C. Coronel,[+] Prof. H. A. Atwater
T. J. Watson Laboratories of Applied Physics
California Institute of Technology Pasadena
CA 91125, USA
E-mail: haa@caltech.edu
Prof. N. S. Lewis
Division of Chemistry and Chemical Engineering
California Institute of Technology
Pasadena, CA 91125, USA
P. Narang, Dr. S. Chen, Dr. J. Yano, Dr. L.-W. Wang, Prof. N. S. Lewis, Prof. H. A. Atwater
Joint Center for Artificial Photosynthesis, CA
E-mail: cshiyou@gmail.com
S. Gul, Dr. J. Yano
Physical Biosciences Division
Lawrence Berkeley National Laboratory
Berkeley, CA 94720, USA
Dr. S. Chen,[+] Dr. L.-W. Wang
Materials Sciences Division
Lawrence Berkeley National Laboratory
One Cyclotron Road, Mail Stop 66, Berkeley, CA 94720, USA
[+]These authors contributed equally to this work

DOI: 10.1002/adma.201304473

© 2013 WILEY-VCH Verlag GmbH & Co. KGaA, Weinheim

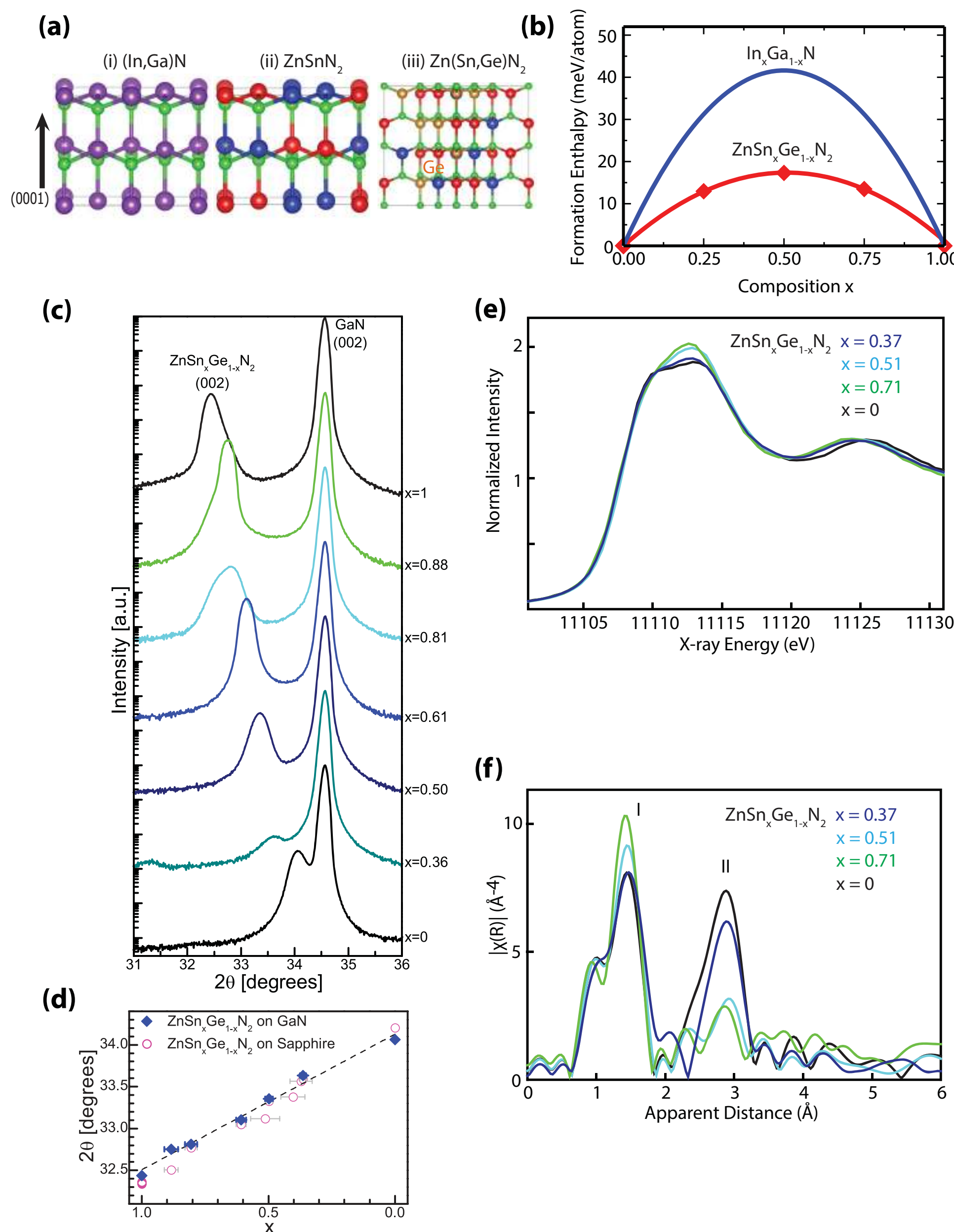

Figure 1. a) The crystal structure of (i) a random $In_xGa_{1-x}N$ alloy, (ii) $ZnSnN_2$ ground-state structure with the $Pna2_1$ symmetry, and (iii) the special quasi-random structure of $ZnSn_{0.5}Ge_{0.5}N_2$. The structures can be derived from the GaN wurtzite structure by replacement of the Ga cations by different cations: (i) In, (ii) Zn and Sn, and (iii) Zn, Sn and Ge; The green, purple, red, blue and yellow balls show the N, Ga (In), Zn, Sn and Ge atoms in order. b) The calculated formation enthalpies of $ZnSn_xGe_{1-x}N_2$ alloys with different compositions x (x = 0, 0.25, 0.5, 0.75 and 1). Sn and Ge atoms are randomly distributed on the Sn sites in the $ZnSnN_2$ structure with $Pna2_1$ symmetry. The red line shows the fit according to Equation 2, with the interaction parameters Ω = 67 meV/atom, and the blue line shows the formation enthalpies of $In_xGa_{1-x}N$ alloys, with the interaction parameter Ω = 166 meV/ atom taken from ref.[7] c) XRD θ-2θ scans around the (002) reflection for films with various compositions grown on *c*-plane GaN template substrates. For comparison, data points are also shown for films grown on sapphire (from ref.[30]) in (d). d) Linear relationship between the (002) peak position and the alloy composition. e,f) Ge K-edge XANES (e) and Ge K-edge FT EXAFS (f) (k^3-weighted) spectra of $ZnGeN_2$ and $ZnSn_xGe_{1-x}N_2$.

alloys must realistically describe the random cation lattice site occupancy for the isovalent elements (Sn and Ge here). Hence we used the well-developed special-quasi-random structures (SQS)[9,10] approach to describe the disordered occupation of Sn and Ge on cation sites. For a given supercell size, special quasi-random structures (SQS) have site occupations (the Sn/Ge sites in the present study) optimized to best reproduce the structural correlation functions of a completely random alloy, so the calculated formation energy and the calculated bandgaps should also be close to those of the random alloys. Figure 1a(iii) illustrates the SQS model having a composition x = 0.5, for which the Sn and Ge were randomized on the 16 Sn/Ge cation sites.

© 2013 WILEY-VCH Verlag GmbH & Co. KGaA, Weinheim
Adv. Mater. **2013**,
DOI: 10.1002/adma.201304473

Detailed structural information of SQS are given in the Supporting Information.

Figure 1b shows the calculated formation enthalpy of the $ZnSn_xGe_{1-x}N_2$ and $In_{1-x}Ga_xN$ alloys, describing the solubility of mixing of Sn and Ge in their sublattice. The formation enthalpy of the alloys is given by:

$$\Delta H_f(x) = E(x) - (1-x)\,E(0) - x\,E(1) \quad (1)$$

where $E(x)$ is the total energy of the alloy having the compositional parameter: $E(0)$ and $E(1)$ are the total energies of $ZnSnN_2$ and $ZnGeN_2$ respectively. The values of $E(x)$ were calculated using standard first-principles methods. The calculated formation enthalpies exhibited an upward bowing in the dependence on the composition, x, indicating that these materials are expected to prefer to phase separate at 0 K into $ZnSnN_2$ and $ZnGeN_2$. The calculated additional energy cost for mixing Sn and Ge cations is given by the calculated formation enthalpies.

To compare these quantities with the formation enthalpies of other alloys, the calculated formation enthalpies were fitted to Equation 2, to yield the interaction parameter, Ω, of the Sn/Ge-mixed alloys:

$$\Delta H_f(x) = \Omega x(1-x) \quad (2)$$

The fit shown by the lines in Figure 1b indicated that the calculated data were in accord with the relationship of Equation 2. The interaction parameter was calculated to be 67 meV/atom (268 meV/mixed-atom). For comparison, Figure 1b also plots the calculated formation enthalpies of the $In_{1-x}Ga_xN$ alloy series using an interaction parameter of 166 meV/atom (332 meV/mixed-atom).[11] The smaller calculated interaction parameter of the $ZnSn_{1-x}Ge_xN_2$ alloys indicates that Sn and Ge are expected to be more easily mixed in the Sn/Ge sublattice than in the In/Ga sublattice of the $In_{1-x}Ga_xN$ alloys. Hence a higher compositional uniformity can be expected in the $ZnSn_{1-x}Ge_xN_2$ alloys relative to that of the $In_{1-x}Ga_xN$ alloys.

The theoretically predicted compositional uniformity of the $ZnSn_{1-x}Ge_xN_2$ alloys was in accord with the structural characterization data of the experimentally synthesized alloys. X-ray diffraction was used to characterize the long-range order of the materials, to thereby determine if the material was a continuous alloy or a mixture of different phases. The observation of a strong peak corresponding to the (002) reflection of $ZnSn_xGe_{1-x}N_2$, coupled with weak peaks or no peaks in any other crystallographic directions, indicated that the films were strongly textured, with the (001) planes oriented parallel to the surface of the substrate. The (002) peak positions for $ZnSnN_2$ and $ZnGeN_2$ were confirmed by calculations based on theoretical lattice parameters (a = 6.70, b = 5.81, c = 5.42 Å for $ZnSnN_2$, and a = 6.39, b = 5.41, c = 5.15 Å for $ZnGeN_2$), and the intermediate compositions of $ZnSn_xGe_{1-x}N_2$ are expected to have peaks with 2θ positions in between those of $ZnSnN_2$ and $ZnGeN_2$.

Figure 1c presents X-ray diffraction θ-2θ scans around the (002) reflection for films with various compositions grown on *c*-plane GaN template substrates. The (002) peak position increased steadily with increasing germanium content in the alloy series, indicating an apparent lack of phase separation in the material. Additionally, the 2θ position of the (002) peak increased monotonically with increasing germanium content, implying that the unit cell continuously expanded and contracted as the composition was changed, which is consistent with the calculated volume change of the alloys with varied composition. Figure 1d further highlights the continuous nature of the alloying of the films, indicated by the linear relationship between the (002) peak position and the alloy composition. Data are shown from many samples with various compositions, with a linear fit of the data for films grown on GaN templates. For comparison, data points are also shown for films grown on sapphire (from ref.[30]). The films grown on GaN were of higher crystalline quality than those grown on sapphire[30] because the lattice mismatch between GaN and $ZnSn_xGe_{1-x}N_2$ is about half of the mismatch between sapphire and $ZnSn_xGe_{1-x}N_2$.

The observed compositional uniformity is in contrast to the behavior of the $In_xGa_{1-x}N$ alloys, in which the large lattice mismatch between InN and GaN causes the indium to segregate, resulting in phase separation and the consequent formation of distinct domains of InN and GaN in alloys with high indium content.[18] X-ray diffraction measurements for phase-separated $In_xGa_{1-x}N$ showed two separate peaks, representing the two different lattice parameters present in the material. In contrast, one prominent peak was observed for $ZnSn_xGe_{1-x}N_2$ in the 2θ range of the (002) reflection, and no peaks were observed at the 2θ positions of $ZnSnN_2$ or $ZnGeN_2$ for films with $0 < x < 1$. The existence of a single (002) peak reinforces the conclusion that $ZnSn_xGe_{1-x}N_2$ is an alloy with continuous variable composition and is not a mixture of different phases. Hence this materials system should allow access to the entire range of bandgap values by use of existing growth strategies.

Figure 1e,f show the Ge X-ray absorption near-edge structure (XANES) and extended X-ray absorption fine structure (EXAFS) spectra of the $Zn(Sn)GeN_2$ alloys as a function of changes in the Sn:Ge ratio. For comparison, the X-ray absorption spectrum of $ZnGeN_2$ is also displayed (Ge K-edge). Although the rising edge energy of Ge stayed constant as the Sn loading increased, the EXAFS spectra clearly showed the structural changes of the alloys. In Figure 1f, the intensity of the first peak that corresponds to the Ge-N interactions increased when the Sn to Ge ratio was increased above 50% (Figure 1d). Additionally, the intensity of the second peak, that contained contributions from Ge-Ge, Ge-Sn, and Zn-Ge interactions around 3.2–3.3 Å (note that the x-axis of Figure 1f is an apparent distance, and it is ~0.5 Å shorter than the actual distances), decreased significantly. The EXAFS curve-fitting results are shown in Figure S1 in the Supporting Information, with the fitting parameters summarized in Table S1 in the Supporting Information. For $ZnGeN_2$, the initial fitting parameters were taken from the crystal structure, and the coordination number (N) was fixed accordingly. The result agrees well with the experimental data (Figure S1c). For $ZnSn_xGe_{1-x}N_2$, a Ge-Sn path around 3.3 Å was included for the curve fitting, and the coordination numbers for the Ge-Ge and Ge-Sn interactions were varied during the fitting. As the fraction of Sn increased, the N number of Ge-Sn increased, while that of Ge-Ge decreased. However, the Debye-Waller factors (σ^2) of the Ge-Ge, Ge-Zn, and Ge-Sn interactions become large in the presence of Sn, as evidenced by the weak peak intensity

© 2013 WILEY-VCH Verlag GmbH & Co. KGaA, Weinheim

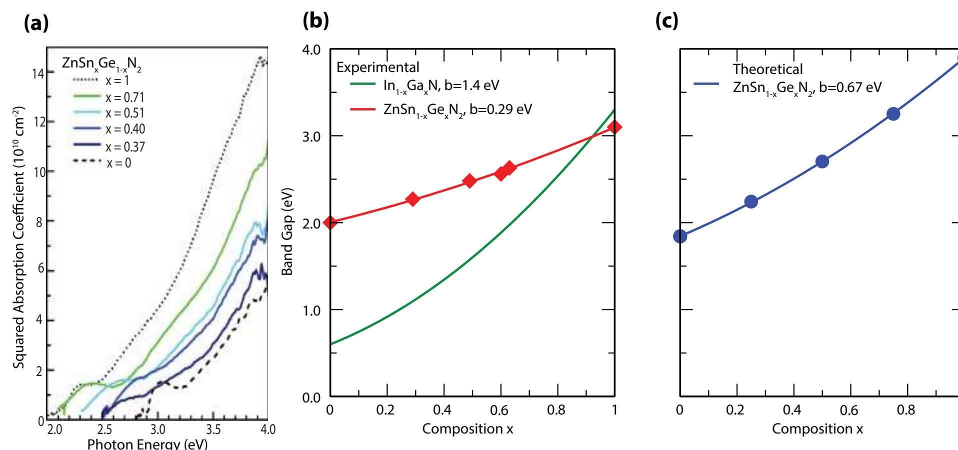

Figure 2. a) Spectroscopic ellipsometry of $ZnSn_xGe_{1-x}N_2$ alloys showing the tunability from 2–3.1 eV of the optical bandgap, as a function of composition in the alloy series. The dependence of the bandgap of the $ZnSn_{1-x}Ge_xN_2$ and $In_{1-x}Ga_xN$ alloys on the composition parameter, *x*: b) experimental data and c) calculated results. The filled diamonds and circles are taken from the experimental measurements and the alloy calculations respectively, and the lines show the fits according to Equation 3. The experimental data for $In_{1-x}Ga_xN$ are from ref.[19]

around the peak II region (Figure 1f). The data therefore indicate that a large distance heterogeneity around 3.3 Å was present in these samples, presumably due to the presence of Ge-Ge, Ge-Zn, and Ge-Sn interactions.

Spectroscopic ellipsometric measurements were used to probe the optical absorption properties of the alloys, particularly near the absorption onset of the materials. The absorption exhibited an obvious blue shift as the Ge composition increased (**Figure 2**a). For direct band-gap semiconductors, the value of the bandgap can be estimated by linear extrapolation to the energy axis of a plot of the square of the absorption coefficient (α^2) versus the photon energy. The fitted gaps are 2.0 eV for $ZnSnN_2$ and 3.1 eV for $ZnGeN_2$. These values are close to those measured previously for different samples, around 2.0 eV (2.0 eV,[8,24] 1.7 eV,[25] and 2.12–2.38 eV)[26] for $ZnSnN_2$ and around 3.2–3.4 eV[25,27,28] for $ZnGeN_2$. As we can see, there is still uncertainty in the exact values of the gaps, but it is safe to say that the gap of $ZnSnN_2$ is around 2.0 eV and that of $ZnGeN_2$ is around 3.2 eV. Figure 2b shows the change in optical bandgap as a function of composition, with the bandgap ranging from 2.0 to 3.1 eV and thereby allowing access to the entire range of bandgaps between $ZnSnN_2$ and $ZnGeN_2$, the two end-point compositions. For comparison, Figure 2b also presents the experimental bandgap change for the $In_{1-x}Ga_xN$ alloys (cited from ref.[19]). The bandgap range spanned by the $ZnSn_{1-x}Ge_xN_2$ alloys (2.0–3.2 eV from the experiments and 1.84 to 3.89 eV from the calculations) is much narrower than that of the $In_{1-x}Ga_xN$ alloys (about 0.6–3.4 eV from experiments). This difference can primarily be related to the higher bandgap of $ZnSnN_2$ relative to that of InN (replacement of two In in InN by Zn and Sn produces an increase of about 1.4 eV in the bandgap).

The bandgap of the alloy series clearly depended nearly linearly on the composition x, as evidenced by the bowing parameter *b*, defined as:

$$E_g(x) = xE_g(1) + (1-x)\,E_g(0) - bx(1-x) \tag{3}$$

A bowing parameter of $b = 0.29$ eV was determined from the measured bandgaps of $ZnSn_{1-x}Ge_xN_2$, whereas a value of $b = 0.67$ eV was obtained from the calculated bandgaps of the same alloy series ($b = 0.3$ eV was also predicted by Punya and Lambrecht for the x = 0.5 alloy),[29] as shown in Figure 2c. Despite an obvious difference, both *b* values are small, and are significantly smaller than *b* for the $In_{1-x}Ga_xN$ alloy series. The small value of *b* indicates that the $ZnSn_{1-x}Ge_xN_2$ alloy bandgaps can be tuned almost linearly by control over the Sn/Ge composition.

Figure 3a,b presents the calculated band structures for the two end-point compounds, $ZnSnN_2$ and $ZnGeN_2$. The two band structures were similar in that both materials have direct bandgaps. Additionally both materials have a lowest conduction band with a large dispersion, with the width of the band about 2 eV, while the highest valence bands are relatively flat in both cases. This behavior is consistent with the orbital component of the two bands (as shown in Figure S2 in the Supporting Information), in that: i) the lowest conduction band is composed mainly of the antibonding state of the hybridization between Sn 5*s* (Ge 4*s*) and N 2*s* orbitals, so this band is delocalized with a significant dispersion, and ii) the highest valence bands are composed mainly of the N 2*p* states, with a weaker hybridization with Zn 3*d* states (because the Zn 3*d* eigen-energy is low and deep in the valence band, the hybridization is weaker, and the Sn 4*d* eigen-energy is much lower, so the hybridization is negligible). Hence the states are localized and have a small dispersion.

The primary difference between the band structure of $ZnSnN_2$ and $ZnGeN_2$ is in the value of the bandgap of each system. Calculations using the hybrid functional (mixing parameter = 0.31) yielded a bandgap of 1.84 eV for $ZnSnN_2$, which is much smaller than the bandgap of $ZnGeN_2$ (3.89 eV).[32] Because both compounds have the top part of their valence bands determined by the N 2*p* and Zn 3*d* states (as shown in Figure S2 of the Supporting Information), the valence band offset should be small. This expectation is

© 2013 WILEY-VCH Verlag GmbH & Co. KGaA, Weinheim
Adv. Mater. 2013,
DOI: 10.1002/adma.201304473

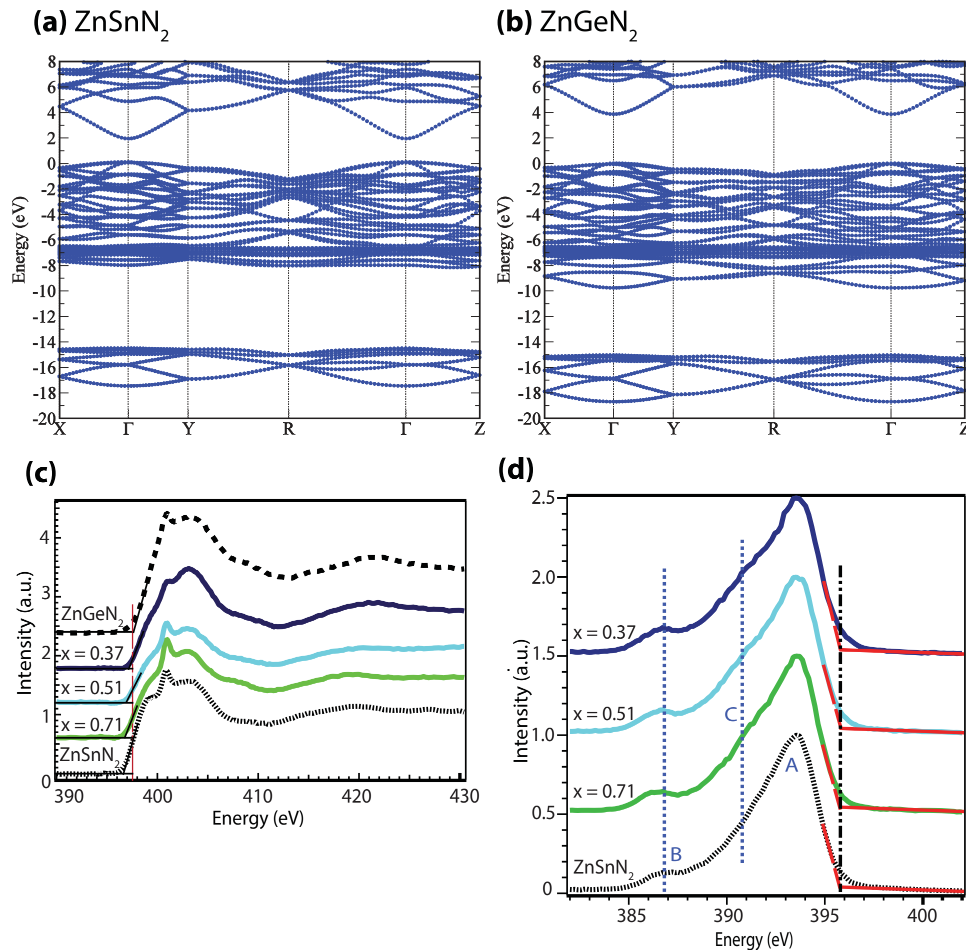

Figure 3. Calculated band structure of: a) $ZnSnN_2$ and b) $ZnGeN_2$, along the high-symmetry lines of the Brillouin zone. c) Nitrogen K-edge XANES spectra for samples with different Ge content as well as the end-point compositions, $ZnSnN_2$ and $ZnGeN_2$. The vertical line (red) indicates the evolution of the conduction-band minimum towards higher energies as a function of increasing Ge content. d) Nitrogen K-edge X-ray emission spectra for samples with different Ge content. As indicated by the vertical line (black), little movement occurred in the valence-band maximum with varying Ge content.

supported by the direct valence band offset calculations, and a valence band offset about 0.4 eV has been found.[31] The much smaller bandgap of $ZnSnN_2$ compared to $ZnGeN_2$ is therefore derived from the much lower conduction-band minimum state, i.e., the large conduction-band offset between $ZnGeN_2$/$ZnSnN_2$. This behavior occurs because the conduction-band minimum state is the antibonding state of Sn 5*s* (Ge 4*s*)+N 2*s* hybridization. In addition, i) the Sn 5*s* orbital energy is much lower than Ge 4*s* orbital energy; and ii) the Sn atom has much larger radius than Ge, so the Sn-N bond length is much larger than the Ge-N bond length, thus the Sn 5*s*+N 2*s* hybridization is weaker than the Ge 4*s*+N 2*s* hybridization, resulting in a lower energy antibonding state for $ZnSnN_2$ relative to $ZnGeN_2$.

Because the band-gap difference is about 1.6–2.0 eV and valence-band offset is only 0.4 eV, we estimate that the $ZnGeN_2$/$ZnSnN_2$ conduction-band offset is large, i.e., larger than 1.2 eV. When the Sn/Ge composition is changed in the $ZnSn_{1-x}Ge_xN_2$ alloys, the bandgap change therefore results mainly from the shift in the position of the conduction band. Furthermore, because the bandgap depends almost linearly on composition, the conduction-band edge should shift almost linearly with the composition parameter, x.

The analysis described above was supported by X-ray spectroscopic data of the electronic structure of these alloys, which was used to complement the spectroscopic ellipsometry data. Ellipsometry is typically restricted to the region close to the bandgap, and provides information about the position of energy levels but does not provide information about the localization or about the orbitals that characterize the electronic states.[12,13] X-ray spectroscopy has element selectivity due to absorption via the core states, whereas chemical sensitivity is obtained due to the participation of valence electrons. Furthermore, due to the dipolar nature of the transitions, particular symmetry information can be obtained. X-ray absorption spectroscopy specifically probes the local unoccupied electronic structure, and is therefore related to the conduction band, whereas X-ray emission spectroscopy (XES) provides information about the local occupied electronic structure, and is therefore related to the valence band. Although the nitrogen *K*-edge XES/XAS spectra do not allow for direct determination of the bandgap, due to the element specificity and selection rules of XES/XAS, the data

© 2013 WILEY-VCH Verlag GmbH & Co. KGaA, Weinheim

do reflect the conduction and valence band characteristics and additionally provide information on the role that specific elements play in determining the electronic structure of the alloys. The spectral features are sensitive to changes in the chemical environment around the element being probed[14,16,17,21] and also provide information about the oxidation state of the absorbing atom, the electronic configuration, and the site symmetry. Thus, X-ray spectroscopy provides a complementary picture of the conduction-band and valence-band states that is distinct from the information obtained via optical transitions. Using the dipole selection rules, the nitrogen *K*-edge XAS involves transitions from localized N 1*s*-like state to unoccupied states with *p*-character in the CB, whereas XES involves transitions from occupied *p* states in the VB to the 1s core hole.

Figure 3c shows the X-ray absorption data for the $ZnSn_xGe_{1-x}N$ samples with varying Sn:Ge ratios, as well as the XAS data for pure $ZnSnN_2$ and $ZnGeN_2$. As indicated by the vertical line, the absorption threshold, which corresponds to the conduction-band minimum, shifted to higher energies as the Ge content increased. For $ZnSnN_2$, the absorption onset was around 396.6 eV whereas for $ZnGeN_2$ the onset was observed at approximately 397.5 eV, with the values for the alloys falling between these two extremes. This behavior is qualitatively consistent with the above analysis based on the large conduction-band offset between $ZnSnN_2$ and $ZnGeN_2$.

Figure 3d presents the N K_α emission spectra, which reflect the valence band partial density of states, for different samples with varying Ge concentration. Figure 3d also presents the X-ray emission spectrum of $ZnSnN_2$. Two features, labeled as A and B, were distinct in all of the spectra, but upon incorporation of Ge, a shoulder labeled as C appeared between A and B, with this shoulder becoming more prominent as the Ge content increased. Feature B also became more pronounced as the Ge content increased. Feature A, appearing at 393.6 eV, mainly corresponds to N 2*p* occupied states, whereas the low energy feature B, that appeared between 386.2 and 386.5 eV originates from nitrogen 2*p* states hybridized with Zn 3*d*, Ge 4*s* and Sn 5*s* states. These assignments are in accord with previous results.[20] The appearance of shoulder C with the addition of Ge is ascribable to the mixing of Ge 4*p* states with N 2*p* states, whereas the enhancement in feature B results from the contribution of Ge 4*s* states. This increase in the partial density of states observed in the lower energy part of the valence band below 392 eV, as displayed by the features B and C, indicates a stronger *s*-*p*-*d* hybridization in case of the alloy samples. As indicated by the vertical black line, the valence-band maximum did not shift upon addition of Ge, which is consistent with the calculated small valence-band offset. Thus, a gradual increase in the bandgap with increasing Ge content primarily occurred by the reorganization of conduction-band minimum to higher energies.

In summary, the experimental observations and first principles calculations of the $ZnSn_xGe_{1-x}N_2$ semiconductors described herein have shown that the alloys can be tuned to span a large portion of the solar spectrum. The bandgap in the $ZnSn_{1-x}Ge_xN_2$ is tunable from 2 eV ($ZnSnN_2$) to 3.1 eV ($ZnGeN_2$), with a linear dependence on the composition arising from the smaller lattice mismatch between $ZnSnN_2$ and $ZnGeN_2$ as compared to the lattice mismatch in the $In_xGa_{1-x}N$ alloys that span the same energy gap range, consistent with theoretical predictions. Thus, the $ZnSn_xGe_{1-x}N_2$ alloys potentially could be useful as earth-abundant light absorbers for artificial photosynthetic devices as well as a replacement for InGaN in nitride-based optoelectronic devices.

Experimental Section

Calculation Methods: The structural relaxation and electronic structure were calculated within the density functional formalism as implemented in the VASP code.[22] For the exchange-correlation potential, both the generalized gradient approximation (GGA) in the PBE form, and the non-local hybrid functional, (HSE)[23] in which 31% (known as the mixing parameter) of the semi-local GGA exchange potential was replaced by screened Fock exchange, were used. For the 16-atom orthorhombic unit cells of $ZnSnN_2$ and $ZnGeN_2$, both the structural relaxation and electronic structural calculations were performed using the hybrid functional calculations. For the structural relaxation of the 64-atom special quasi-random structure (SQS) for the $ZnSn_xGe_{1-x}N_2$ alloys, the structural relaxation was performed using the PBE functional, due to the heavy calculation cost of the hybrid functional. The following electronic structure calculation was also performed using the hybrid functional. The *d* states of the group II and IV elements were treated explicitly as valence. The interaction between the core electrons and the valence electrons was included by the standard frozen-core projector augmented-wave potentials. An energy cut-off of 400 eV was applied in all cases. For Brillouin-zone integration, k-point meshes that were equivalent to the 6×6×6 Monkhorst-Pack meshes for a 16-atom orthorhombic unit cell were used. All lattice vectors and atomic positions were fully relaxed by minimization of the quantum mechanical stresses and forces.

Experimental Methods:

Deposition via Reactive RF Magnetron Sputtering: Thin films were synthesized in an AJA International sputtering chamber (base pressure 10^{-8} Torr) from a combined $Zn_{0.75}Sn_{0.25}$ target and an elemental Ge target in an Ar/N_2 gas mixture (3 mTorr) with varying power on the Ge target to vary the composition. The films were deposited on *c*-sapphire and LUMILOG *c*-GaN template substrates.

X-ray Spectroscopy: X-ray spectroscopic data were collected at the Advanced Light Source (ALS) at Lawrence Berkeley National Laboratory, with an electron energy of 1.9 GeV and an average current of 500 mA.

Soft X-Ray Measurements: Nitrogen *K*-edge XAS and XES measurements were performed using beamline 7.0.1. The beamline was equipped with a 99-pole, 5 cm period undulator and a spherical grating monochromator,[15] and delivered intense radiation with a narrow band-pass.

For X-ray absorption, the beamline resolution was set to 0.15 eV at 400 eV. Spectra were recorded in total electron yield (TEY) mode by measurement of the sample drain current and total fluorescence yield (TFY) mode using a channeltron. The incident photon energy was calibrated by measurement of the X-ray absorption spectrum of hexagonal boron nitride (BN) during the experiment. The spectra were normalized to the photocurrent produced by a gold mesh that was inserted in the beamline between the last mirror and the sample. The incident radiation had a linear *p*-polarization (E vector in the plane of incidence), and samples were oriented at a grazing incidence with an angle of 20° with respect to the incident beam.

X-ray emission spectra were recorded using a grazing incidence spectrometer[16,17] that had a resolution of 0.4 eV at the N *K*-edge.[21] With a Rowland circle geometry, the spectrometer consisted of a 20 µm wide and 2 cm long entrance slit, a spherical grating with a 5 m radius and 1200 lines mm^{-1}, and a two-dimensional detector. The emission spectra were measured with the spectrometer mounted at angle of 90° relative to the incident beam. The emission energies were calibrated using the elastic peaks of emission spectra of the N *K*-edge that were produced by the BN reference sample. All data were collected at room temperature.

© 2013 WILEY-VCH Verlag GmbH & Co. KGaA, Weinheim
Adv. Mater. **2013**,
DOI: 10.1002/adma.201304473

Hard X-Ray Measurements: Hard X-ray absorption spectra (XAS) were collected at beamline 10.3.2. The radiation was monochromatized by a Si (111) double-crystal monochromator. The intensity of the incident X-ray beam was monitored by use of a N_2-filled ion chamber (I_0) positioned in front of the sample. Fluorescence spectra were recorded using a seven-element Ge solid-state detector. The monochromator energy was calibrated relative to the rising-edge energy of a Ge foil (11103.00 eV). Data reduction of the XAS spectra was performed using custom-made software (Matthew Marcus). The pre-edge and post-edge contributions were subtracted from the XAS spectra, and the results were normalized with respect to the edge jump. Background removal in *k*-space was performed by use of a five-domain cubic spline. Curve fitting was performed with Artemis and IFEFFIT software using ab initio calculated phases and amplitudes from the program FEFF 8.2. The details of the curve fitting are discussed in the Supporting Information.

X-Ray Diffraction (XRD): The structure and phase of the II-IV nitrides was evaluated by XRD obtained using a PANalytical X'Pert diffractometer with a Cu K α source ($\lambda = 1.5406$ Å), over a 2θ range of 30° to 43° for the thin films on a c-plane-oriented sapphire substrate.

Ellipsometry: Spectroscopic ellipsometry was performed on samples grown on c-sapphire. Data were collected at an incidence angle of 70° for 250 nm < λ < 2300 nm, with a Xe lamp visible light source and a Fourier-transform infrared spectrometer. The value of the bandgap is estimated by linear extrapolation to the energy axis of a plot of the square of the absorption coefficient (α^2) versus the photon energy as is typical for direct band-gap semiconductors.

Supporting Information

Supporting Information is available from the Wiley Online Library or from the author.

Acknowledgements

This material is based upon work performed by the Joint Center for Artificial Photosynthesis, a DOE Energy Innovation Hub, supported through the Office of Science of the U.S. Department of Energy under Award Number DE-SC0004993, and was also supported by the Dow Chemical Company. P.N. acknowledges support from a National Science Foundation Graduate Research Fellowship and from the Resnick Sustainability Institute. X-ray spectroscopy work was performed at the Advanced Light Source (ALS, BL 10.3.2 and 7.0.1), Berkeley, under Contract DE-AC02–05CH11231. The authors thank Drs. Jinghua Guo and Per-Anders Glans-Suzuki for their support at BL 7.0.1.

Received: September 5, 2013
Published online:

[1] S. Nakamura, S. J. Pearton, G. Fasol, *The Blue Laser Diode: The Complete Story*, 2nd ed., Springer, Berlin **2000**.
[2] I. Vurgaftman, J. R. Meyer, *J. Appl. Phys.* **2003**, *94*, 3675.
[3] J. Wu, W. Walukiewicz, W. Shan, K. M. Yu, J. W. Ager, S. X. Li, E. E. Haller, H. Lu, W. J. Schaff, *J. Appl. Phys.* **2003**, *94*, 4457.
[4] N. Duxbury, U. Bangert, P. Dawson, E. J. Thrush, W. Van der Stricht, K. Jacobs, I. Moerman, *Appl. Phys. Lett.* **2000**, *76*, 1600.
[5] Z. Liliental-Weber, D. N. Zakharov, K. M. Yu, J. W. Ager, W. Walukiewicz, E. E. Haller, H. Lu, W. J. Schaff, *J. Electron Microsc.* **2005**, *54*, 243.
[6] S. Chen, X. G. Gong, A. Walsh, S.-H. Wei, *Phys. Rev. B* **2009**, *79*, 165211.
[7] S. Chen, A. Walsh, Y. Luo, J.-H. Yang, X. G. Gong, S.-H. Wei, *Phys. Rev. B* **2010**, *82*, 195203.
[8] L. Lahourcade, N. C. Coronel, K. T. Delaney, S. K. Shukla, N. A. Spaldin, H. A. Atwater, *Adv. Mater.* **2013**, *25*, 2562.
[9] A. Zunger, S.-H. Wei, L. G. Ferreira, J. E. Bernard, *Phys. Rev. Lett.* **1990**, *65*, 353.
[10] S.-H. Wei, L. G. Ferreira, J. E. Bernard, A. Zunger, *Phys. Rev. B* **1990**, *42*, 9622.
[11] K. Biswas, A. Franceschetti, S. Lany, *Phys. Rev. B* **2008**, *78*, 085212.
[12] F. de Groot, *Chem. Rev.* **2001**, *101*, 1779.
[13] J. Stöhr, *NEXAFS Spectroscopy, Springer Series in Surface Sciences, Vol. 25*, Springer **2003**.
[14] J. J. Rehr, R. C. Albers, *Rev. Mod. Phys.* **2000**, *72*, 621.
[15] T. Warwick, P. Heimann, D. Mossessian, W. McKinney, H. Padmore, *Rev. Sci. Instrum.* **1995**, *66*, 2037.
[16] J. Nordgren, G. Bray, S. Cramm, R. Nyholm, J. E. Rubensson, N. Wassdahl, *Rev. Sci. Instrum.* **1989**, *60*, 1690.
[17] P. Bennich, T. Wiell, O. Karis, M. Weinelt, N. Wassdahl, A. Nilsson, M. Nyberg, L. G. M. Pettersson, J. Stöhr, M. Samant, *Phys. Rev. B* **1998**, *57*, 9274.
[18] R. Singh, D. Doppalapudi, T. D. Moustakas, L. T. Romano, *Appl. Phys. Lett.* **1997**, *70*, 1089.
[19] J. Wu, *J. Appl. Phys.* **2009**, *106*, 011101.
[20] A. Punya, W. R. L. Lambrecht, M. van Schilfgaarde, *Phys. Rev. B* **2011**, *84*, 165204.
[21] J. J. Yeh, I. Lindau, *Atomic Data and Nuclear Data Tables* **1985**, *32*(1), 1–155.
[22] G. Kresse, J. Furthmueller, *Phys. Rev. B.* **1996**, *54*, 11169.
[23] J. Paier, M. Marsman, K. Hummer, G. Kresse, I. C. Gerber, J. G. Angyan, *J. Chem. Phys.* **2006**, *124*, 154709.
[24] N. Feldberg, B. Keen, J. D. Aldous, D. O. Scanlon, P. A. Stampe, R. J. Kennedy, R. J. Reeves, T. D. Veal, S. M. Durbin, in *Proc. 38th IEEE Photovoltaic Specialists Conf. (PVSC)* **2012**, p. 2524.
[25] P. C. Quayle, K. He, J. Shan, K. Kash, *MRS Commun.* **2013,** FirstView 1.
[26] N. Feldberg, J. D. Aldous, W. M. Linhart, L. J. Phillips, K. Durose, P. A. Stampe, R. J. Kennedy, D. O. Scanlon, G. Vardar, R. L. Field III, T. Y. Jen, R. S. Goldman, T. D. Veal, S. M. Durbin, *Appl. Phys. Lett.* **2013**, *103*, 042109.
[27] K. Du, C. Bekele, C. C. Hayman, J. C. Angus, P. Pirouz, K. Kash, *J. Cryst. Growth* **2008**, *310*, 1057.
[28] S. J. Pearton, M. E. Overberg, C. R. Abernathy, N. A. Theodoropoulou, A. F. Hebard, S. N. G. Chu, A. Osinsky, V. Fuflyigin, L. D. Zhu, A. Y. Polyakov, R. G. Wilson, *J. Appl. Phys.* **2002**, *92*, 2047.
[29] A. Punya, W. R. L. Lambrecht, in *Proc. Int. Conf. Silicon Carbide and Related Materials* **2011**, Materials Science Forum, Volume *717–720*, p. 1331.
[30] N. C. Coronel, L. Lahourcade, K. T. Delaney, A. M. Shing, H. A. Atwater, in *Proc. 38th IEEE Photovoltaic Specialists Conference (PVSC)* **2012**, p. 003204.
[31] A. Punya, W. R. L. Lambrecht, *Phys. Rev. B* **2013**, *88*, 075302.
[32] A comparison of the calculated and experimental bandgaps of $ZnSn_{1-x}Ge_xN2$ alloys indicates a departure of calculated values from those observed experimentally. Specifically, the calculated bandgap of ZnGeN2 is about 0.7 eV larger than the experimental value, while the calculated value of ZnSnN2 is 0.16 eV smaller than the experimental value, even though the same calculation methods (the mixing parameter = 0.31 in the hybrid functional) were used for both materials systems. To make sure that our main conclusions about the bandgaps do not depend on the specific calculation methods, we also calculate the bandgap bowing parameter and valence band offset between $ZnGeN_2/ZnSnN_2$ using the normal generalized-gradient approximation (GGA), a small bandgap bowing parameter and a small valence band offset are also found.

© 2013 WILEY-VCH Verlag GmbH & Co. KGaA, Weinheim